Sensing and Imaging (2026) 27:76
https://doi.org/10.1007/s11220-026-00771-1

RESEARCH

# High-Sensitivity D-Shaped Fiber Optic Plasmonic Sensor Using Hybrid Grating Structure for Refractive Index Detection

**Pooria Rabiei[1] · Kiana Peyvandi[2] · Ali Asghar Ajami[3] · Mohammad Danaie[1]**

Received: 7 February 2026 / Revised: 7 February 2026 / Accepted: 21 March 2026


## Abstract
This study introduces a surface plasmon resonance-based fiber optic sensor (SPR) designed to accurately detect the refractive index of the environment. The sensor structure is based on a D-shaped fiber, with thin layers of gold, titanium dioxide and silver applied successively to its flat surface. To increase the optical coupling, a nanometre grating is also used on the upper layer of silver. Numerical simulation with the finite element method (FEM) was performed to optimize the spectral response of the analysis sensor and structural parameters. The results show that the sensor has a sensitivity of 5100 nm/RIU and a half-height bandwidth of about 14.5 nm. Its FOM number reaches 351.7 $RIU^{-1}$, which performs better compared to many fiber-based SPR sensors. The sensitivity analysis to fabrication tolerances has also shown that the proposed design is resistant to small changes. Due to its simple and feasible structure with conventional techniques, the sensor can be used in applications such as water quality monitoring, biodegradation and environmental analysis.

**Keywords** Optical fiber sensor · Surface plasmon resonance · Water quality monitoring

✉ Mohammad Danaie
danaie@semnan.ac.ir

[1] Department of Electrical and Computer Engineering, Semnan University, Semnan, Iran

[2] Faculty of Chemical, Petroleum and Gas Engineering, Semnan University, Semnan, Iran

[3] Faculty of Physics, Semnan University, Semnan, Iran

Published online: 10 April 2026

## 1 Introduction

The phenomenon of surface plasmon resonance has become one of the most widely used tools in the fields of optical scattering for physical, chemical and biological parameters since the late 1970s. Surface plasmon waves are electromagnetic waves that can exist at the boundary between a metal (or any other dissipative medium with sufficient free electron density) and a dielectric [1–3]. These waves can only be excited by a p-polarized incident wave (i.e. a wave whose electric field component lies in the plane of incidence) [4–6] and propagate along the boundary between the two media [7, 8]. The electromagnetic field of this type of wave decays exponentially in both media (metal and dielectric) [9, 10]. When the constant parallel component of the incident light wave is equal to the constant real part of the surface plasmon wave, the surface plasmon is excited resonantly, and as a result, the power of the reflected wave is greatly reduced [11–13].

The surface plasmon resonance (SPR) condition is very sensitive to changes in the refractive index of the surrounding medium (which is usually the same analyte under investigation and in contact with the metal surface) [14–16]. This property allows the analyte—often a liquid—to be identified by a change in its refractive index, which is observable by a shift in the minimum reflected power (resonance dip) [17]. Refractive index sensors (RI sensors) are an efficient option for industrial applications due to their simple design and compact structure [18, 19]; Especially in areas such as quality control, production process monitoring, food industry and environmental pollution monitoring. From a scientific perspective, these sensors have also found wide applications in areas such as chemical and biological analysis, medical applications, and sample identification [20–22].

This combination of research and operational applications, along with high measurement accuracy, has made refractive index-based sensing technology one of the key approaches in the development of ultra-sensitive sensors [23, 24].

In 2020, Agharazy Dormeni and colleagues designed and simulated a sensor based on SPR and LSPR that uses gold nanostructures. In this study, types of thin-layer structures including flat surface, nanoparticles, cubic nanoparticles, and nanowires were examined and simulations were performed with COMSOL software. The best performance was for an array of 20 nm cylindrical nanowires on a 40 nm gold layer, which achieved a peak sensitivity of 4916 nm/RIU and an average of 5847.2 nm/RIU in the breakdown index range of 1.333 to 1.38. However, the design presented is purely theoretical and lacks empirical validation. The sensor also faces serious construction challenges due to the need for precise shaping and uniformity of intermittent nanostructures. In addition, the paper did not examine tolerance analysis, optical losses or the possibility of connecting this structure to optical fiber platforms, which limits its practical application in real conditions [25].

In 2020, Lu Kong and colleagues designed an SPR sensor using graphene and sub-longitudinal silver gratings. The structure used a BK7 prism, two 15-nm silver layers, and a graphene layer to optimize plasmonic coupling. Simulations showed that by carefully tuning the grating parameters, very low reflectance ($2.9 \times 10^{-6}$), narrow spectral width (~3.5 degrees), and a maximum sensitivity of 220.67 degrees per RIU in the range of 1.333 to 1.36 could be achieved.

Despite the improved performance, this design also faces limitations. The use of a prism and a precise goniometry method make it difficult to integrate it into fiber-optic or portable systems. Also, the sensor requires advanced processes such as creating nanometer-scale double-layer gratings and precise graphene placement, which are difficult to implement on an industrial scale. On the other hand, the performance of the device depends on the uniformity of the graphene thickness, and a slight deviation in the fabrication process can lead to a loss of sensitivity [26].

In 2020, Kadhim and Al-Hemeary designed a D-shaped fiber optic-based SPR sensor using silver nanowires (AgNWs) to improve detection sensitivity and accuracy. The sensor structure consisted of single-core optical fiber with a core of 9 and a coating of 125 micrometers, the surface of which was prepared with a lateral polishing technique and nanowires with a radius of 40 to 70 nanometers were indicated on it. The results of the FEM simulation showed that with a radius of 60 nm and a residual thickness of 0.4 micrometers, the highest sensitivity is equal to 5.1 µm/RIU in the breakdown index range of 1.35 to 1.39. Despite its very good performance, to make this sensor, it is necessary to implement the precise removal of the coating layer and the uniform insertion of nanowires, which poses challenges in the construction process [27].

In 2022, Maya Chauhan and her colleagues designed a D-shaped fiber-based optical sensor with a semi-internal microchannel that uses the phenomenon of surface plasmon resonance (SPR) to detect the refractive index of the medium. The structure of this sensor consisted of a single-mode optical fiber with a germanium-doped silica core polished to a depth of 25 µm and a 10 µm-wide microchannel etched into its surface with a distance of only 0.2 µm from the core. A 50 nm-thick gold layer was placed at the bottom of the microchannel to create an active plasmon region and provide direct interaction between the light guided in the core and the analyte sample. This design was done with the aim of reducing manufacturing costs and achieving appropriate sensitivity, and the results of finite element method (FEM) simulations showed a sensitivity of 1757 nm/RIU in the range of 1.33 to 1.38. However, despite the structural innovation, this sensor faces some practical limitations.

Its fabrication process requires precise etching of a very narrow microchannel with submicron accuracy near the core, which is difficult to control reproducibly and may introduce fabrication errors. In addition, the placement of the sample inside the channel makes the washing and reuse process difficult, limiting its application in variable flow conditions or environments. Also, although a remarkable sensitivity is reported, this paper does not mention the figure of merit (FOM) or the unexcited spectral width, which is of great importance for evaluating the accuracy of the sensor in real applications [28].

In 2023, Sharma and colleagues designed a D-shaped fiber-based SPR sensor to detect ethanol, which uses a combined coating of gold, graphene, and molecular molded polymer (MIP). The sensor structure included a nuclear with germanium doping, a gold layer 40 nanometers thick, a graphene layer 7 nanometers thick, and a MIP layer 10 nanometers thick. FEM simulation and experimental results showed a sensitivity equal to 714 nm/RIU for AU/MIP structure and 1137 nm/RIU in the presence of graphene.

Despite improvements in sensitivity and build capability, this sensor also has limitations. Its design is optimized solely for the detection of ethanol and its performance against other analyses or real biological samples has not been investigated. Also, the average competence number (23.8) and separability in the range of 10 − 4 to 10 − 6 RIU are relatively limited compared to more advanced designs. Failure to check the tolerability of changing the thickness of the layers may also affect the repeatability of the construction [29].

In the study of Rahad et al., a MIM waveguide is introduced along with the ring structure and silver metal, which has a sensitivity of about 2783 nm/RIU. Despite its proper spectral performance, the sensor requires a high-temperature (160 ° C) and high-pressure (50 bar) lithographic process, which faces problems such as lack of uniformity, unwanted layer residue, and limitations in repeatability.

In addition, the structure does not have the ability to carry and use in real space due to its large dimensions and lack of integration with fiber [30]. In the article Haque, Mohammad Ashraful, et al., using silver nanoparticles, the sensitivity of 2975.96 nm/RIU and FOM is reported to be about 26.32 RIU − 1. However, the structure's dependence on the location of nano points, the stimulation of high-order mods and high sensitivity to input conditions undermine the stability of the sensor's operation under operating conditions. Also, the design lacks checking for construction errors and optical strength that prevent widespread use [31].

In 2024, Hosea and Rugumira presented a charter-based SPR sensor with a four-layer structure of CaF2, TiO2, Ag and BaTiO3 that used divergent beams to detect heavy metals in water. The sensor achieved a sensitivity of 399.45 degrees on the RIU in the limited range of the refractive index (1.3317 to 1.34). Despite improvements in the coupling with the help of dielectric layers, its design depends on precise beam adjustment and angular detection with CCD, which makes it difficult to implement in portable or real-time systems. Also, the lack of optical fiber and high intensification width (~ 2.17 degrees) limits its accuracy and practical flexibility [32].

Kadhim et al. presented a D-shaped fiber-based sensor with microchannels and $WO_3$-coated Ag/Au bimetallic layers, which achieved wavelength sensitivities of 6000 and 5000 nm/RIU (for Au and Ag, respectively) and FOMs of 50.12 and 134.84. However, this structure not only lacked any experimental validation, but also the design of its micro-hollow channels required precise microfluidic technologies and dedicated equipment, which makes mass production difficult. Also, the high thickness of the metal oxide layers reduces the depth of field penetration and the detection accuracy is degraded [33].

In Tuaimah et al., an optical crystalline fiber (PCF) based SPR sensor with D-shaped polish and double-layer TiO2/Au coating is presented, which aims to simultaneously identify multiple analytes. Despite innovative conceptual design, the paper lacks numerical data such as sensitivity, FOM or FWHM, and performance evaluation is provided only qualitatively. Also, the construction of PCF fiber with a square grid requires advanced technologies such as precision traction and capillary layout, which limits its construction on a real scale. The proposed structure lacks parametric tolerance analysis and empirical evaluation, and the modal response or sustainability of its performance against construction deviations has also not been investigated. These factors reduce reliability and practical implementation [34].

A dual channel SPR Fiber sensor has been developed by Yan et al. that allows for the simultaneous determination of Glutathione (GSH) concentration and liquid Refractive Index (RI) of a liquid. The sensor consists of two multimode fibers that are connected by a TCF. Each multimode fiber is constructed from a different material: one section is coated with an Au/MnO2 bilayer and the other is coated with an Indium Tin Oxide (ITO)/Silver bilayer. The GSH sensitivity was found to be −2.361 nm/mM over the concentration range of 0.005 to 50 mM and the RI sensitivity was found to be 1704.252 nm/RIU within the range of 1.331 to 1.3895 RIU.

The experimental results showed that the sensor had good reproducibility and good selectivity to common interferents. In fact, the MnO2 film was found to increase the GSH sensitivity by a factor of approximately 25 compared to an uncoated Au fiber and also allowed for dual channel detection with very low crosstalk. Unfortunately, the resonance linewidth was found to be very broad and there was no attempt to specifically design the sensor for optimal FWHM vs. sensitivity trade-off or to use a D-shape fiber. These advantages motivate further, unique designs for SPR fiber sensors that will have improved FOMs and higher spectral resolution for the measurement of RI [35].

The work by Sun et al. uses both a no-core fiber and a bubble formation to develop a dual-parameter fiber optically based SPR sensor with an extremely narrow full width at half maximum of the resonance dip. This work demonstrates that the change of the glass medium to create a bubble in the structure will allow for the modulation of the angle of incidence of light at the metal interface, resulting in a decreased FWHM of the resonance dip associated with the dual-parameter SPR sensor.

Both segments of these sensors consist of Ag-coated no-core fiber. Ag-coated no-core fiber segments are used for determining the index of refraction of the solution over an index of refraction range of 1.333–1.385 and Ag/PDMS-coated no-core fiber segments are used for the temperature detection over a temperature range of 0–50 °C. These segments are spliced to multimode fibers resulting in a compact probe design.

By optimizing the bubble size, the researchers lowered the FWHM value from 83 nm to 58 nm and achieved RI sensitivity values as high as 3715.3 nm/RIU between the ranges of [2.6, 3.7] and temperature sensitivity values as high as 3.9 nm/°C for the range of temperatures tested from [0 °C, 50 °C]. Both of these sensors have been demonstrated to have low limits of detection and excellent repeatability. Although this work provides a significant decrease in the FWHM of the resonance dip in a dual-parameter SPR fiber sensor, it does not utilize a D-shaped fiber with engineered multilayers and does not utilize a combined multilayer/grating design to improve sensitivity, FOM, and manufacturing tolerances of single-parameter refractive index sensors [36].

In their work, Rutirawut et al. developed a compact Kretschmann-type SPR sensor that incorporates a polarization controlled beam of light from a fiber into a BK7 prism and a reattachable sensing chip made from a 2 nm thick film of Cr and a 40 nm thick film of Au on the surface of the prism. The optimal prism angle (63.5°) and thickness combination (Cr: Au = 2:40 nm) resulted in a narrow deep SPR dip in the region of Near-infrared (NIR) with an ultra-high simulated sensitivity of 34 888 nm/RIU in the region of 1.3235 to 1.3290 RIU, as well as experimental determination of saline (455 nm/M) and sucrose concentration (3056 nm/M) using the device.

As a re-usable sensing chip incorporated into a fiber-optic design, this Kretschmann-type sensor provides a flexible, miniaturised alternative to bulk Kretschmann-type sensors. The sensor, however, continues to use a prism-coupled planar sensor design rather than an all-fiber D-shaped configuration and this work does not consider incorporating dielectric layers or surface gratings to manipulate field confinement and full-width half-maximum (FWHM) in the optics of the fiber itself, which is the aim of the current potentially hybrid multimode D-shaped fiber sensor [37].

Chakraborty et al. achieved an extraordinary sensitivity of 130,000 nm/RIU and the sensitivity of the 1939.83 RIU − 1 skirts, using D-shaped D-core design and TiO2/Au layers. However, this structure requires special fibers with parallel cores, bilateral polishing and high alignment accuracy, which limits its implementation to advanced laboratory environments. In addition, the article does not report on the medial response and structural stability against environmental fluctuations [38].

Despite significant achievements in optical sensors based on SPR, some problems remain. Many previous studies have focused on improving sensitivity by changing the integration of nano substances such as plasmon layers, or optimizing the structure of fibers. However, most of the current methods require more complex fabrication processes or use expensive materials, which makes their large-scale implementation challenging. Also, some studies have achieved high sensitivities, but have compromised the detection accuracy due to increased optical absorption losses and large resonance peak widths [39–41].

In order to address the above limitations, we propose a D-shaped fiber SPR sensor that combines a compact Au/TiO2/Ag multilayer stack with a shallow surface grating fabricated directly on the polished region of a standard silica fiber. In contrast to previously reported D-shaped SPR sensors that either use simple metal–dielectric coatings or grating-assisted coupling alone, the present hybrid multilayer–grating configuration simultaneously tailors field confinement and phase matching while keeping the overall structure compatible with conventional fiber polishing and thin-film deposition. By properly choosing the thicknesses of the Au, TiO2 and Ag layers and optimizing the grating depth and period, strong plasmonic coupling is achieved with reduced optical losses, leading to a narrow resonance dip and a high figure of merit (FOM).

Numerical modelling based on the finite-element method (FEM) in COMSOL Multiphysics is employed to evaluate the spectral response of the sensor over a wide refractive-index range relevant to water-quality and biochemical monitoring. Compared with many existing SPR fiber sensors, which typically trade high sensitivity for broader resonance peaks or rely on complex special fibers and nanofabrication steps, the proposed design offers an improved balance between sensitivity, spectral resolution and fabrication practicality [42, 43]. The main novelties and contributions of this work can be summarized as follows.

(i) We design a D-shaped SPR fiber sensor that integrates an Au/TiO2/Ag multilayer with an on-fiber shallow grating, enabling simultaneous enhancement of plasmonic field confinement and coupling efficiency in a structure that can be realized using standard D-shaped fiber polishing and thin-film coating techniques. (ii) We demonstrate, through full-vector FEM simulations, a high wavelength sensitivity of 5100 nm/RIU and a FOM of 351.7 $RIU^{-1}$ with a narrow FWHM of 14.5 nm over the refractive-index range 1.31–1.37, which is highly relevant for water-quality monitoring and other liquid-phase sensing applications. (iii) We perform a detailed parametric and fabrication-tolerance analysis, showing that the sensor performance is robust against ± 5 nm deviations in the thicknesses of the Au, TiO2 and Ag layers, which is crucial for reliable and reproducible experimental implementation [44–46].

The proposed sensor structure, the underlying theoretical model and the numerical analysis of its performance are presented in the following sections.

## 2 Theoretical Background

Surface plasmon resonance (SPR) is an important optical phenomenon occurring at the interface between metal and dielectric, making possible the use of sensitive refractive index (RI) sensing. The effect is produced when the incident p-polarized-light couples with free electrons in the metal, forming surface plasmon waves. The resonance condition is finely attuned to the dielectric properties of the surrounding medium, which makes SPR sensors exquisite for detecting minute changes in RI. In order to analyse the performance of the proposed sensor, we need to derive key plasmonic equations that include the dispersion relation for surface plasmons, the resonance condition, and the effective refractive index. Moreover, parameters, such as sensitivity (S), figure of merit (FOM), and full-width at half maximum (FWHM), will be introduced in order to characterize sensor performance. In due course, the theoretical setup of SPR, along with the governing equations and analytical framework, will be presented to set the ground for numerical modelling.

The SPR optical structure consisted of a metal-dielectric boundary that allowed the passage of a p-polarized electromagnetic wave, which propagated along the boundary as a surface plasmon wave (SPW). Intense absorption of light occurred due to energy transfer during the collision, which resulted in a decrease in the energy of the reflected light. As a result, the resulting spectrum was an evanescent wave that behaved similarly to an SPW. The following Eq. (1) gives the resonance condition:

$$K_{SPW} = K_0\left(\frac{\varepsilon_{mr} n_s^2}{\varepsilon_{mr} + n_s^2}\right)^{1/2} \tag{1}$$

Where $K_0 = \frac{2\pi}{\lambda}$ The propagation constant (KSP) with $\varepsilon_{mr}$as the dielectric constant of the metal, and the right-hand side of the relation represents the real part of this constant. Also, $n_s$represents the refractive index of the dielectric layers (sensor). This technique is very effective for detecting and sensing various variables, because the matching condition related to this diffusion constant has a high sensitivity to optical changes in the dielectric constant [8, 47, 48].

Sensor sensitivity (S) is one of the most important performance metrics for surface plasmon sensors, indicating the amount of shift in the resonance wavelength in response to changes in the refractive index of the medium. This value is expressed in nanometres per refractive index unit (nm/RIU) and is calculated from Eq. 2, where $\Delta\lambda_{res}$ indicates the change in the resonance wavelength and Δn is the amount of change in the refractive index of the medium. The higher the sensitivity value, the more accurately the sensor detects smaller changes in the refractive index.

$$\mathrm{S} = \frac{\Delta\lambda_{res}}{\Delta \mathrm{n}} \tag{2}$$

The spectral width at half maximum (FWHM) is one of the key parameters in the spectral analysis of sensors, which expresses the width of the resonance peak at the point where the signal intensity has decreased to half of the maximum value. The FWHM value has a direct impact on the spectral resolution accuracy and detection accuracy of the sensor; The lower this value is, the higher the sensor's spectral resolution and the higher its ability to detect very small changes in the environment. This value is usually extracted from the reflectance or optical transmission curve of the sensor, in such a way that first the signal maximum is determined and then the two points where the signal intensity is reduced to half the maximum are known as the FWHM limits.

The full width at half maximum (FWHM) of the resonance was determined directly from the transmission spectra T(λ), where the SPR response appears as a well-defined transmission dip. For each spectrum, the minimum transmission (T_min) and the maximum transmission (T_max) were identified. The half-depth level was then computed as (Eq. 3):

$$T_{1/2} = T_{\min} + \frac{1}{2}(T_{\max} - T_{\min}) \tag{3}$$

The wavelengths at which T(λ) = $T_{1/2}$ were obtained on both sides of the dip by linear interpolation. The difference between these two wavelengths defines the FWHM. This method is consistent with standard practice in fiber-optic SPR sensors and allows for a robust comparison of resonance sharpness across different layer thicknesses.

FWHM is also a measure of the sensor's ability to detect small changes in the refractive index of the environment. Another parameter, the resolving power (DA), is defined as the reciprocal of the FWHM value and is calculated according to Eq. (4). A higher DA value indicates that the sensor is more accurate in detecting small changes in the refractive index. In surface plasmon sensors, decreasing the FWHM value leads to an increase in DA, thereby improving the sensing performance [49–51].

$$\frac{1}{\mathrm{FWHM}} = \mathrm{DA} \tag{4}$$

One of the important metrics used to characterize the performance of a surface plasmon sensor is the sensor sensitivity divided by the full-width at half maximum (FWHM) (see Eq. 5). The FOM applies to both of the sensor's key aspects, high sensitivity as well as adequate spectral resolution. Generally, the greater the FOM value then the more sensitive the sensor will be to small changes in the refractive index. Generally, devices with large FOM values will tend to have greater accuracy in detecting change and will be much more useful to biological, medical and environmental applications where estimate changes refractive index needs to be measured rapid and accurately.

$$\frac{\mathrm{S}}{\mathrm{FWHM}}=\mathrm{FOM} \tag{5}$$

The effective refractive index is a fundamental quantity in the characterization of optical waveguides and surface plasmon sensors. It defines the average refractive index of the wave that propagates in the optical structure. The effective refractive index will be defined on the basis of the waveguide structure and the properties of the materials contained within it, the dispersion of the material, and the wavelength of radiation; it will also change along with the refractive index of the sensing medium. This parameter is analysed using the characteristics of the electromagnetic field in the optical structure and solving the phase matching condition between the infiltrated incoming light and the surface plasmon wave. In SPR sensors, analysing the effective refractive index in terms of how it changes when the refractive index of the medium changes contributes to assessing sensitivity and overall performance. The greater the change in the refractive index of the medium, the greater the electromagnetic field interact in the medium, which contributes to sensitivity of the sensor. The value can be calculated from Eq. 6.

$$n_{eff} = \frac{\beta}{k_0} \tag{6}$$

In Eq. (6), $\beta$ is the wave propagation constant in the sensing medium and $k_0$ is the wave number in vacuum.

The specified value was then used to evaluate the optical transmission characteristics and sensing performance of the sensor. In this stage, the light transmission rate in a given wavelength range was analysed and normalized transmitted power was calculated using Eq. (7).

$$T = \exp(-\frac{4\pi}{\lambda_0} imag(n_{eff}) L) \tag{7}$$

In Eq. 7, T is the normalized light transmission, $\lambda_0$ is the wavelength of the source light, $imag(n_{eff})$ is the imaginary part of the effective refractive index, which represents the amount of energy loss and light absorption by the sensor, and L is the sensor length. This equation shows that decreasing the value of $imag(n_{eff})$ increases the transmission power and improves the sensor performance. Here, $n_{\text{eff}} = n' + k$ is the complex effective index of the plasmonic mode. The imaginary part $n''$ quantifies the intrinsic attenuation of the mode due to metal absorption, producing an exponential decay of the intensity along the propagation direction. The interaction length was set to $L = 1\,\text{mm}$, corresponding to the physical length of the polished D-fiber sensing region. This length ensures that the plasmonic attenuation yields a measurable resonance dip while maintaining sufficient transmitted power [52].

## 3 Methods

This study reveals the design and simulation of a new SPR sensor based on D-shaped optical fiber. The D-shaped optical fiber was chosen for this construction due to the flat surface of the fiber which allows room for the guided light in the waveguide to interact with the external environment directly. This construction allows for more sensitivity in the sensors ability to detect small changes in the refractive index of the external medium. D-shaped optical fibers are increasingly used for the design of SPR sensors, because of their high light guiding capacity and ability to utilize the external environment. One of the crucial points in designing this sensor was the fabrication of layers of gold, silver, and $TiO_2$. Gold was chosen for the base metal layer because of its unique plasmonic properties. Gold is able to create strong, stable surface plasmons that assist with accurately determining a change in the refractive index. Silver was chosen to act as an amplifier in the structure because silver has even stronger plasmonic properties than gold. Silver can increase the strength of surface plasmons, providing a substantial increase in sensor sensitivity. The $TiO_2$ layer was selected as the intermediate layer for its high refractive index and mechanical and chemical resistance. The intermediate layer provides higher optical coupling and reduces oxidation of the silver layer. One primary goal during the design of this sensor was to maximize sensitivity. Therefore, a grating structure fabricated on the silver layer was used in the design process to increase the interaction of oncoming light and surface plasmons and reduce optical noise. The structure of the grating (periodicity and depth of the lines) influenced sensor performance immensely.

This structure is designed in such a way that it can analyze different wavelengths of light and detect small changes in the refractive index of the environment with high accuracy. Another important aspect in the design of this sensor was the accurate analysis of the refractive indices of different aqueous environments. The refractive indices of drinking, industrial, and muddy waters are in the range of 1.31 to 1.37. These refractive indices have a direct impact on the plasmonic resonance and light transmission coefficient in the sensor.

The shallow surface grating that would be necessary in the designed configuration ($\Lambda = 200$ nm, $h = 50$ nm) is well within the capabilities of modern nanofabrication technologies, as demonstrated by the D-shaped fibre having a polished area that provides a quasi-planar surface for the application of planar fabrication techniques, including electron beam lithography, nano imprint/conformal imprint lithography, and focused ion beam milling. All of these techniques have been demonstrated in practice to produce metallic sub-wavelength gratings for surface plasmon resonance (SPR) sensing applications [47, 52]. Furthermore, similar grating-assisted SPR devices have been previously reported in the literature, including D-shaped fibres with Ag/α-$Fe_2O_3$ coatings, suggesting that it is feasible to fabricate a 200 nm period, 50 nm depth grating onto the D-shaped fibre.

In this study, a comprehensive numerical analysis was conducted to evaluate the optical performance of the proposed surface plasmon resonance-based optical sensor (SPR). The purpose of the simulations was to investigate the sensor spectral response under different conditions of the refractive index and structural configurations. For this purpose, the Finite Element Method (FEM) method was used in the

COMSOL Multiphysics software environment, which was selected due to its high ability to model the interaction of electromagnetic fields and multilayer nanostructures. The computational domain was modeled in two dimensions and was used to remove artificial reflections and increase the accuracy of the analysis, in the upper and lower edges of fully adapted layers (PML) and in the sides of the domain scattering Boundary Condition (Scattering boundary Condition). For accurate sampling of rapid changes in the electric field at the boundary between metal and dielectric, a physical-controlled triangular mesh was applied and locally thinned in critical areas. In the final simulation, more than 20,000 mesh elements were produced with an average quality of 0.88 and the sustainability of the results was examined with a convergence test.

The structure optimization process was performed as a parametric analysis on key design variables including gold layer thickness (20–60 nm), TiO2 (5–20 nm) and silver (10–40 nm), grating period (400–800 nm), grating height (30–90 nm) and grating distance from the core. In each configuration, parameters such as resonance wavelength displacement, bandwidth at semi-maximum (FWHM), sensitivity ($S=\Delta\lambda/\Delta n$) and competence number ($FOM=S/FWHM$) were calculated and compared to select a structure with optimal performance.

Although the focus of this study is numerical modeling, the proposed design is also consistent with conventional construction processes. The D-shaped geometry of the fiber can be created by mechanical polishing, metal layers can be applied through physical vapor coating (PVD) or sputtering, and surface grating can be implemented with lithography methods such as nanoimprint or electron-beam lithography. These features make the design presented a practical option for experimental implementation and future development.

## 4 Sensor Design and Structure

The D shaped optical fiber contains a silica core and cladding layer; the manufacturing process removes part of the cladding to create a flat surface with access to the cladding and core of the fiber. The light that is guided in the fiber core will have the ability to interact directly with the environment because of the open pull the D shaped optical fiber incurs with a flat surface. The radius of the fiber core is 5 μm and the cladding radius is 62.5 μm. Surface grating is 200 nm spacing and 50 nm height with two sections that are 25 nm height. The dimensions are specifically calculated so that the light continues to be guided in the fiber while increasing the amplitude of the optical field. The flat surface of the D-shaped optical fiber is made by removing part of the cladding and the top parts of the cladding and core form a high-level supported surface for metal and dielectric deposition. In practical fabrication, a thin adhesion layer is typically required between the silica surface and the gold film to ensure mechanical stability and avoid delamination. Common choices include 1–3 nm of Cr or Ti, which significantly improve gold adhesion while introducing negligible optical loss due to their ultrathin thickness relative to the SPP skin depth. This approach has been widely used in fiber-based plasmonic structures and is fully compatible with the proposed multilayer design.

**Table 1** Sellmeier coefficients for the fiber core and cladding

| Coefficient | $a_1$ | $a_2$ | $a_3$ | $b_1(\mu m)$ | $b_2(\mu m)$ | $b_3(\mu m)$ |
|---|---|---|---|---|---|---|
| Clad | 0.6961663 | 0.4079426 | 0.8974794 | 0.0684043 | 0.1162414 | 9.896161 |
| Core | 0.7028554 | 0.4146307 | 0.8974540 | 0.0727723 | 0.1143085 | 9.896161 |

**Table 2** Optical material parameters used in simulations

| Material | Optical data source | Spectral range of *n*, k data | Notes |
|---|---|---|---|
| Au (Gold) | Babar & Weaver (2015) | 0.2066–12.40 µm | Experimental refractive index & extinction coefficient; widely used plasmonic model |
| $TiO_2$ (Titanium dioxide) | Sarkar et al. (2019) | 0.30–1.69 µm | Thin-film optical constants; suitable for dielectric coatings |
| Ag (Silver) | Wu et al. (2014) | 0.29–1.00 µm | Measured n, k data; optimized for plasmonic applications |

The optical fiber structure used in this study includes a core and sheath of melted silica (SiO2), which is common in the design of standard multimode fibers. It is considered a suitable option for optical sensors due to its low optical losses, high chemical stability and wide transparency window. In this study, the core and optical fiber sheath are considered to be germanium-alloyed silica (GeO2) and pure silica, respectively, in line with the common designs of multi-mode optical fibers with a stair profile. The wavelength-dependent failure coefficient for both the core and sheath segments is calculated using the sellmeier scattering interface, which is in [52] Presented:

$$n(\lambda) = (1 + \frac{a_1\lambda^2}{\lambda^2 - b_1^2} + \frac{a_2\lambda^2}{\lambda^2 - b_2^2} + \frac{a_3\lambda^2}{\lambda^2 b_3^2})^{1/2} \tag{7}$$

where the Sellmeier coefficients are represented by b3, b2, b1, a3, a2 and a1, and the wavelength is represented by $\lambda$. This study utilised the parameters shown in Table 1:

The proposed sensor structure consists of three main layers, which are respectively placed on the flat surface of the optical fiber (Table 2):

The gold layer is the initial metal layer that is deposited directly on the flat surface of the optical fiber. The thickness of this layer was made 30 nm. Gold was selected as the base metal due to its exceptional plasmonic properties, chemical stability, and superior resistance to oxidation. The 25 nm thick $TiO_2$ layer is used as an essential dielectric between the metal layers. The layer was selected due to its high refractive index and mechanical durability. $TiO_2$ contributes to increasing surface plasmon field intensity and sensor sensitivity. A 25 nm thick silver layer is added as the top layer in the structure. Silver was chosen based on its superior plasmonic properties compared to gold and its ability to form the highest plasmonic field intensity. As the top layer it also interacts directly with the external environment. Figure 1 shows the proposed structural design of the SPR based fiber optic sensor and demonstrates how the lay-

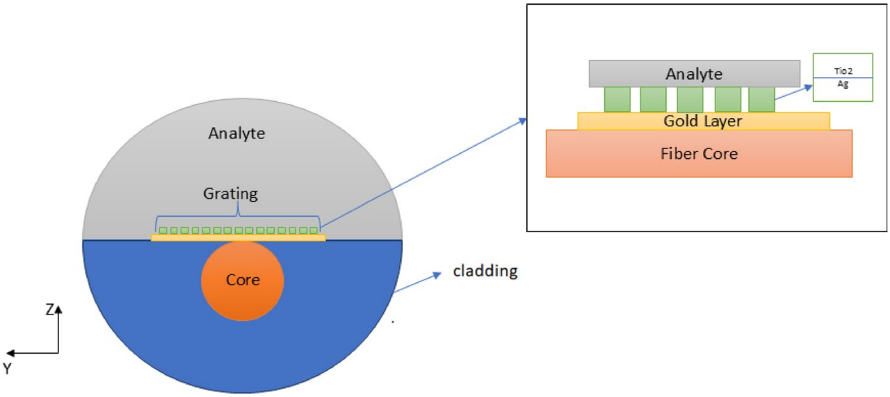


**Fig. 1** Provides a cross-sectional view denoting placement of the grating on the fiber structure and its configuration with the analyte. The design also facilitates enhanced sensitivity through the exploitation of plasmonic resonance effects

ered structure interacts with the analyte. The coefficients of mixed refraction (n and k) for gold (Au), silver (AG) and titanium dioxide (TiO2) were extracted directly through the material Library in COMSOL Multiphysics version 6.1. The refractive index of $TiO_2$ was taken from the COMSOL material library, which corresponds to the rutile phase of $TiO_2$. These data are presented as a function of wavelength based on experimental measurements in the spectral range and are used through internal functions in the simulation environment to model optical behavior and dispersion of materials with high accuracy. A 2D cross-sectional eigenmode model of the D-shaped fiber was employed. The metal–dielectric multilayer and surface grating are located on the polished flat surface of the D-fiber; given the large fiber radius (~62.5 µm) compared to the nanoscale grating features and SPP penetration depth, the local interface can be approximated as planar, and curvature effects are neglected.

For a detailed analysis of the sensor, various optical and geometric parameters were considered in the simulations. The wavelength of the input light was set in the range of 600 to 1150 nm and the refractive indices of different media (1.31 to 1.37) were applied. Also, the absorbing boundary condition (PML) was added to the model to prevent unwanted reflections and increase the accuracy of the simulation. The input light was defined as polarized (TM-mode) to optimize the effect of surface plasmons. These settings not only increased the accuracy of the simulation, but also helped to analyze the optical behavior of the sensor under different conditions. One of the main challenges in optical simulations is managing unwanted reflections at the model boundaries. To prevent these reflections, Perfectly Matched Layer (PML) were used. These boundary conditions allow the software to fully absorb electromagnetic fields that pass through the model boundaries. A 2D cross-sectional eigenmode analysis was carried out in COMSOL Multiphysics. The computational domain was a circular region of 80 µm radius (slightly larger than the 62.5 µm cladding radius), with a scattering boundary condition at the outer edge. The fundamental core-guided mode was solved and its complex effective index was used to compute the resonance wavelength and confinement loss.

In the numerical simulation process of surface plasmon resonance-based fiber optic sensors, meshing is one of the key steps that affects the accuracy and efficiency of modeling. Meshing means dividing the computational domain into smaller elements in which the numerical equations are solved with higher accuracy. In this simulation, a non-uniform mesh has been used in which sensitive areas such as the metal-dielectric contact surface (the site of surface plasmon excitation) have been meshed with smaller elements to achieve higher accuracy in solving the equations. In contrast, in areas further away from the metal surface, coarser elements have been used to reduce the computational load. Figure 2 illustrates the meshing configuration used in the simulation, ensuring accurate numerical analysis by optimizing element distribution across the sensor structure.

A significant aspect of this research was the sensor design optimization to increase sensitivity, minimize spectral width at half maximum (FWHM), and maximize sensor performance. At the time, key parameters affecting sensor performance were investigated including metal layer thickness, grating periodicity, and the refractive index of the sensing medium. All these parameters govern the optical properties of the sensor

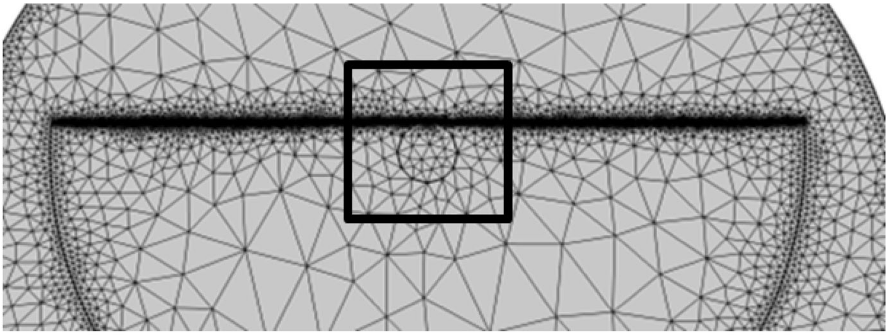

(a)

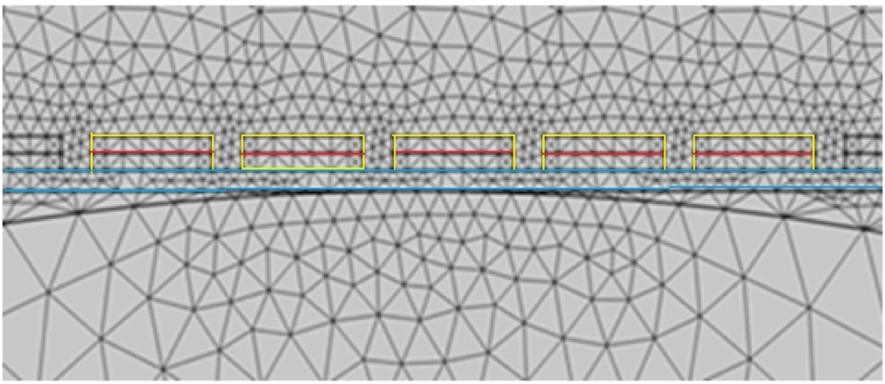

(b)

**Fig. 2** Mesh generation for the proposed SPR-based sensor model. The meshing process is refined to enhance computational accuracy, particularly in regions with high field variations, ensuring precise simulation of plasmonic interactions. **a** mesh overview and **b** Meshing close-up and their optimal value could play a substantial role in the efficiency of the sensing system. The first parameter to change was the metal layer thickness which was varied in 5 nm steps from 10 to 50 nm, as this was one of the primary components of the sensor. The research was conducted to establish the effect of the metal layer thickness on the wavelength of the resonance and amount of light absorption. The study revealed that at a metal layer thickness of 30 nm maximal sensitivity was obtained and a metal layer thickness of 34 nm resulted in maximum light absorption. Increasing the metal thickness beyond the optimal range leads to increased losses from the metal, resulting in decreased sensitivity of the sensor, while decreasing metal thickness down to certain limits the intensity of the resonance signal decreased due to decreased plasmonic coupling. Thus, the suitable thickness of gold was found to range from 30 to 34 nm depending on whether accuracy or absorption rate was prioritized.

A mesh-convergence study at $n_a = 1.33$, using six mesh levels between $6.0 \times 10^4$ and $2.9 \times 10^5$ domain elements, showed that the resonance wavelength remained fixed at 825 nm for all meshes, while the minimum transmission varied by less than 4% (see Table 3), confirming mesh-independent results.

The grating periodicity was also another important variable in sensor design. The effect of the periodicity value on sensor performance was assessed by altering its value. Varying the grating periodicity can alter the position of the resonance wavelength and increase or decrease sensitivity of the sensor. The analyses show that at a specific value of the periodicity the best plasmonic coupling is obtained, which causes the largest shift of the resonance wavelength in response to changes in the refractive index of the medium. The refractive index of the sensing medium is also another factor affecting sensor performance, and by changing it, the sensitivity and spectral response of the sensor change. In this study, the refractive index of the medium was varied in a specific range from 1.31 to 1.37 and its effect on the resonance wavelength position and sensor sensitivity was investigated.

In addition, two different approaches to optimization were investigated. In one of these cases, changing the thickness of the gold layer produced the highest optical absorption, but the sensor accuracy decreased. In contrast, in the case where the thickness of the silver and TiO2 layers was adjusted, the absorption decreased slightly but the sensor accuracy increased significantly. The analyses showed that the sensor had the highest accuracy at a thickness of 25 nm of silver and 25 nm of titanium dioxide, while the highest absorption was observed at a thickness of 20 nm of silver and 30 nm of titanium dioxide.

**Table 3** Mesh-convergence analysis of the FEM model for the proposed D-shaped SPR sensor, showing the variation of the resonance wavelength as a function of mesh density in the sensing region. The small change in λ_res for finer meshes confirms the numerical stability of the simulation results

| Mesh level | Domain elements | Boundary elements | Resonance wavelength λ_res (nm) | T at λ_res (–) |
|---|---|---|---|---|
| Extremely coarse | 60,332 | 7,590 | 825 | 0.4853 |
| Coarser | 93,074 | 8,188 | 825 | 0.4805 |
| Normal | 124,272 | 8,264 | 825 | 0.4692 |
| Finer | 142,512 | 8,339 | 825 | 0.4692 |
| Extra fine | 165,220 | 8,364 | 825 | 0.4700 |
| Extremely fine | 287,004 | 8,564 | 825 | 0.4662 |

To make the optimization procedure more transparent, the influence of the $TiO_2$ layer thickness on the spectral characteristics of the SPR resonance is summarized in Fig. X. The $TiO_2$ thickness is varied from 5 nm to 45 nm in steps of 5 nm at an analyte refractive index of n_a = 1.33, and the corresponding FWHM, absorption depth (1 − T_min) and resonance wavelength λ_res are plotted.

As seen in Fig. 3a, the FWHM exhibits a clear minimum of about 20–25 nm around TiO2 ≈ 25 nm, while significantly larger values are obtained for non-optimal thicknesses such as 15 nm. Figure 3b shows that the resonance remains sufficiently deep in the range 10–25 nm, but becomes much shallower for thicker $TiO_2$ layers (> 35 nm). Meanwhile, Fig. 3c indicates a monotonic shift of λ_res towards shorter wavelengths as the $TiO_2$ thickness increases. These trends demonstrate that a $TiO_2$ thickness of approximately 25 nm provides a favorable trade-off between narrow linewidth, strong resonance and a convenient operating wavelength, and this value is therefore used in the final optimized sensor design.

Combining all these results, it was found that the highest sensor accuracy was achieved at a thickness of 30 nm of gold with 25 nm of silver and 25 nm of titanium dioxide, while the highest absorption occurred at a thickness of 34 nm of gold and 20 nm of silver and 30 nm of titanium dioxide. These analyses showed that choosing the design parameters in such a way that a balance between optical absorption and sensor accuracy can ensure the most optimal performance. All these analyses were carried out in the form of a parametric study to determine the best combination of parameters to achieve optimal sensor performance. The final value of each parameter was selected based on a comparison of the sensor performance under different conditions, and these values were used in the final simulation stage. This optimization process allowed us to adjust the sensor design in such a way that, in addition to increasing the sensitivity and detection accuracy, the spectral response was also optimized. The results of this optimization will be examined in the next chapter to determine the extent of the improvement in sensor performance. The optimized structural parameters of the designed fiber-optic sensor, based on surface plasmon resonance, are presented in Table 4. These parameters have been selected to maximize sensitivity and absorption efficiency.

## 5 Results and discussions

To investigate the distribution of the electric field in the sensor structure, the distribution of the field intensity (|E|) at the resonance wavelength was calculated for several different refractive indices. This analysis shows how the electric field is concentrated at the metal surface and adjacent layers of the sensor. The simulation results showed that at the refractive index $n = 1.33$, the electric field intensity reaches its maximum value near the metal surface. This increase in field intensity is due to the optimal conditions for surface plasmon excitation in this range. Since the field distribution at different refractive indices shows similar behavior, only the image corresponding to $n = 1.33$ is shown to avoid repetition of similar images. These images are considered representative of the field distribution in the entire sensor structure, and other refractive indices have a similar effect on the field behavior.

**Fig. 3** Dependence of the SPR spectral characteristics on the $TiO_2$ layer thickness at n_a = 1.33: **a** FWHM of the resonance dip, **b** absorption depth (1 − T_min), and **c** resonance wavelength λ_res. The results indicate an optimal $TiO_2$ thickness of about 25 nm, which yields a narrow linewidth and a sufficiently deep resonance

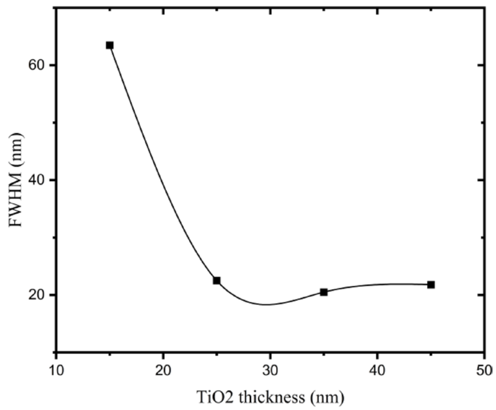


(a)

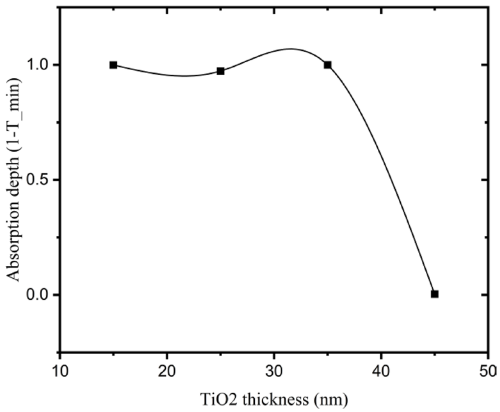


(b)

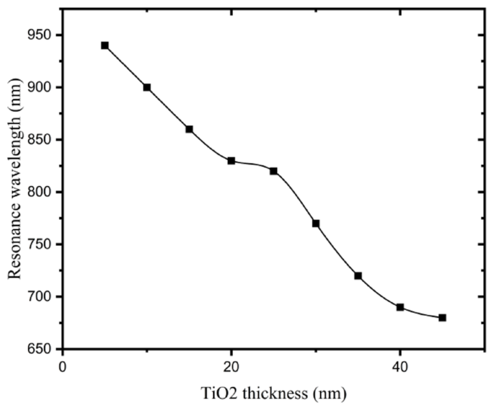


(c)

**Table 4** Optimized design parameters of the fiber-optic sensor based on surface plasmons, including variations for maximum sensitivity and absorption efficiency

| Parameter | Optimization range | Optimized value for maximum sensitivity | Optimized value for maximum absorption |
|---|---|---|---|
| Core radius (um) | 5 | | |
| Cladding radius (um) | 62.5 | | |
| Wavelength of light (nm) | 600–1150 | | |
| Gold layer thickness (nm) | 10–50 | 30 | 34 |
| Grating layer thickness (nm) | 50 | | |
| Silver layer thickness (nm) | 5–40 | 25 | 20 |
| TiO2 layer thikness (nm) | 5–40 | 25 | 40 |
| Grating period (nm) | 50–500 | 200 | 200 |

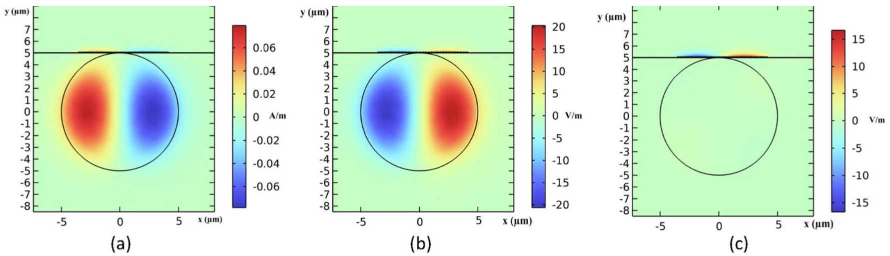


**Fig. 4** Distribution of electromagnetic field components in the sensing region. **a** Magnetic field Hx distribution. **b** Transverse electric field Ey distribution. **c** Longitudinal electric field Ez distribution

Figure 4 shows the distribution of electromagnetic field components in the sensor area. In Figure 4a, the transverse magnetic component Hx shows a symmetrical distribution relative to the fiber cross section, where a phase change is observed near the Common Core–Metal season. This pattern indicates the presence of transverse magnetic modes and their interaction with the metal plasmon layer. Figure 4b shows the transverse electric field Ey, concentrated mainly in the fiber core area and uniformly reduced towards the outer layers. This distribution indicates proper waveguide behavior and low field leakage, which is necessary for effective coupling with plasmon mods. In Figure 4c, the longitudinal component of the EZ electric field is most concentrated in the upper area of the sensor, that is, in the common metal–dielectric season. The high intensity of the field in this area indicates strong stimulation of surface plasmon mods and energy concentration at the sensor boundary, which is a confirmation of the surface-sensitive optical response of the structure.

This set of Fig. 5 shows the outer distribution of electromagnetic field components in an SPR sensor of a D-shaped fiber with a grating structure. Compared to the localized plots, these plots give a broader spatial overview of the way the fields propagate and decay in the outside region.

Figure 5a indicates the transverse magnetic field (Hx), and field lines are depicted diverging symmetrically about the core region. The accumulation at the metal-dielectric interface, with a subsequent slow decay outward, is evidence of the presence of well-confined plasmonic surface modes. The high magnetic coupling is a sign of good interaction with incoming light and maximum energy confinement. Figure 5b

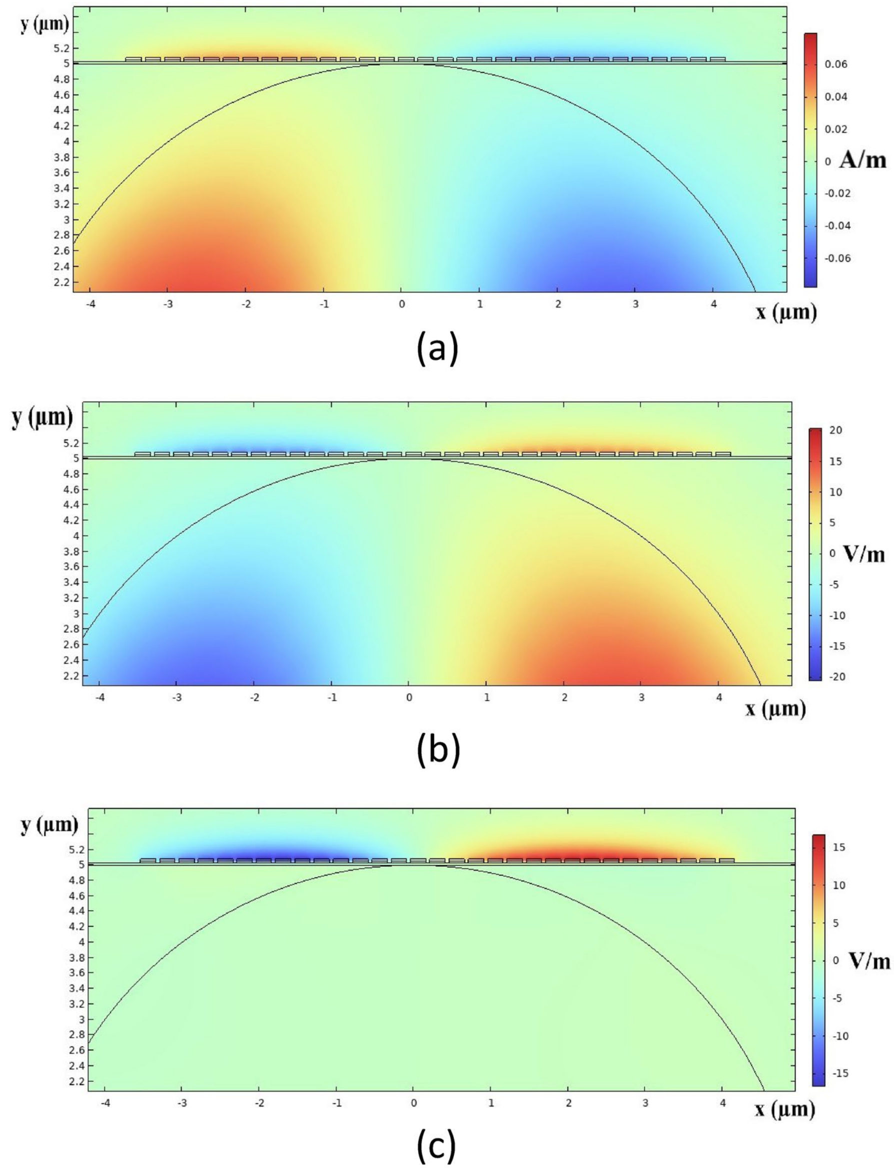


**Fig. 5** Outer distribution of electromagnetic field components in the D-shaped fiber sensor structure. **a** Transverse magnetic field Hx, **b** Transverse electric field Ey, **c** Longitudinal electric field Ez

is the Ey component, and it displays intense concentration of intensity on the top and bottom sections of the structure. The pattern confirms strong grating layer coupling and effective excitation of transverse guided modes. Symmetry in the pattern also indicates structural stability and effective light confinement inside the sensing region. Figure 5c reveals the Ez component of the electric field, which is fundamentally the one responsible for exciting SPR mainly in the propagation direction. High energy localization near the top metal layer is a sign of localized surface resonance and maximum overlap between the guided light and the metal interface and hence higher sensor sensitivity and resolution.

Figure 6 efficiently displays the transmission spectrum curves for different refractive index parameters, specifically RI = 1.31 to RI = 1.37. This demonstrates the extent to which the refractive index for the surrounding medium can influence the characteristics of SPR resonance peaks, including their position, intensity, and shape. Along with the observation of the resonant peak shifting to longer wavelengths (redshift) with increased refractive index, the sensor is demonstrated to have enough sensitivity to be able to measure changes in refractive index. An increase in dissolved material or contamination is represented as a distinct shift in the resonance peaks. In this case, the lower refractive index is represents a shift in resonance wavelength around 750 nm (about the refractive index of pure water) toward 950 nm at the greatest refractive index represented by $n = 1.37$ (indicating polluted or concentrated solutions). Another obvious trend is the increased spread of the resonance peaks as measured by Full Width at Half Maximum (FWHM) with increased refractive index. As the refractive indices increase, the peaks broaden meaning more energy loss in the SPR mode and less resolution for the sensor due to higher concentrations or contaminates. However, the depth and strength of transmission loss stays reliable and consistent as you can see throughout the refractive indices measured, and even with the peak widening, lengthening or reappearance of transmission losses, the singles remain well-oriented for a reliable sensor. Also, we can see differences in spacing between resonance peaks for refractive indexes measured. The spacing measurements are much greater at lower refractive indexes (like values between $n = 1.31$ and $n = 1.34$) and cards in spacing at higher refractive indexes (like values between $n = 1.35$ and $n = 1.37$), as it is clear from the analysis that the sensor demonstrates its greatest sensitivity at lower refractive indices.

The Fig. 7 shows how light behaves for two refractive indices: RI = 1.34 and RI = 1.341, which are very similar. Even though the difference is very little (0.001 RIU), the sensor still recognizes this change. We see this change because the posi-

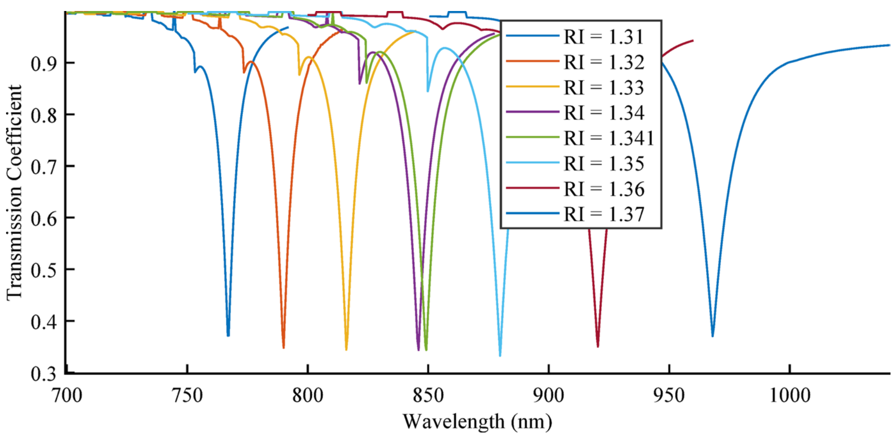


**Fig. 6** Studying the trend of changes in surface plasmon resonance peaks at different refractive indices

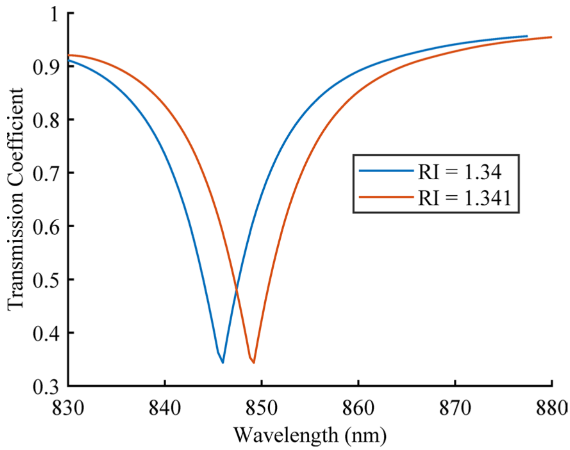


**Fig. 7** Examination of the transmission coefficient of two refractive indices of 1.34 and 1.341, which shows the resolving power of the sensor

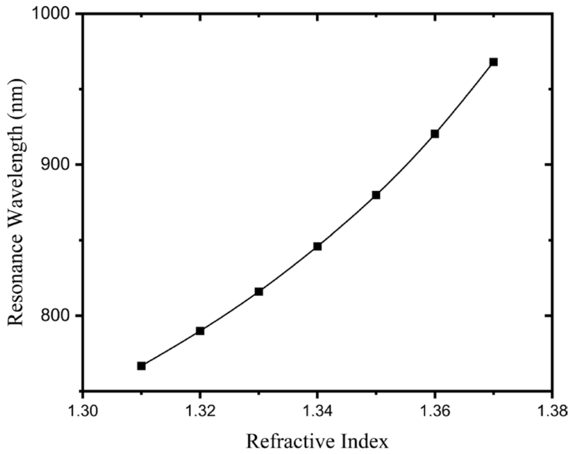


**Fig. 8** Change in resonance wavelength depending on the refractive index of the medium

tion of peaks is moving since light resonates at different locations. For an RI = 1.34, the resonance peak appears around 849 nm, once the refractive index moves slightly higher (RI = 1.341), the resonance peak appeared at ~851 nm. This movement indicates that the sensor is very sensitive, demonstrating that it is able to detected tiny, minute changes in the RI of the surrounding medium. This level of sensitivity is important for applications that require precision, such as monitoring minor variations in water quality, early detection of environmental pollutants, and monitoring chemical solutions. Thus, this sensor provided a better performance than other commercially available sensors that have been previously mentioned.

Figure 8 shows the relationship between the resonance wavelength and the environmental failure coefficient. As can be seen, as the refractive index increases from 1.31 to 1.37, the resonance wavelength increases continuously and relatively nonlinear. This behavior is caused by the high sensitivity of the structure to environmental changes and the strong coupling of plasmon modes with an optical field, which are known features of SPR sensors. The highest wavelength shift occurs in the range of

1.35 to 1.37, indicating a reinforced response in the more sensitive area of the structure. According to the graph, the sensitivity value is calculated on average equal to approximately 5100 nm/RIU, which confirms the optimal performance of the sensor in detecting very small changes in the refractive index.

Figure 9 shows bandwidth changes in the semi-maximum (FWHM) as a function of the environmental failure coefficient. This parameter is one of the key indicators in evaluating the performance of surface plasmon-based optical sensors, as it is directly related to the resolution and accuracy of the detection. In the designed structure, the value of FWHM varies between about 6.5 and 9.6 nm in the breakdown index range 1.31 to 1.37, which is scientifically acceptable and indicates the formation of narrow and powerful intensification peaks in the transit spectrum. The graph shows that at some points such as RI = 1.341, despite increased sensitivity, the FWHM value remained almost constant, indicating the presence of an exacerbation with a high Q-factor in that area. In general, the decrease in FWHM indicates an increase in the resolution of the resonant peak and an improvement in the detachability of the sensor. On the other hand, the direct relationship between FWHM and the competence number (FOM) also confirms that in points with less FWHM, the overall performance of the sensor will be more optimal in terms of accuracy and responsiveness to environmental changes. Numerical precision and uncertainty. The transmission spectra were determined using COMSOL simulations between 600 and 1150 nm, using a local sampling interval of approximately 1 nm near the location of SPR dips and sweeping the analyte RI in steps of 0.01 RIU from 1.31 to 1.37.

Using the minima of the transmission spectra, the wavelengths of the resonance and FWHM were determined through linear interpolation, and the sensitivity value was obtained through linear regression of $\lambda\_res$ and RI datasets. Given the spectral and RI resolutions, the numerical uncertainty associated with the calculated wavelengths, FWHM, and sensitivities, were $\Delta\lambda\_res \leq \pm 0.5$ nm; ΔFWHM; and ΔS, ≈ ±50 nm/RIU; therefore, the total error of the measured FOMs is ≈ ± 30 1/RIU (FOMs, ≈ 351 ± 30 1/RIU). The uncertainties stated are sufficiently small such that they do not affect the relative ordering of the values provided in the optimization results section.

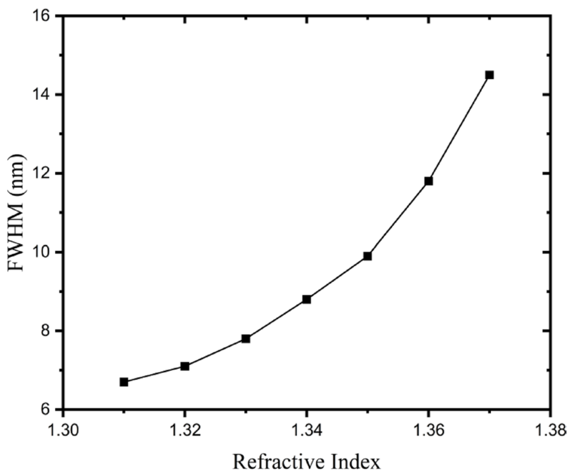


**Fig. 9** The spectral width of the resonance at the dip point is an important measure of the sensor's detection accuracy. A lower FWHM means a sharper optical response and better performance

To evaluate the spectral behavior of the sensor with respect to the changes in the refractive index of the environment, the calibration plot between the resonant wavelength and the refractive index of the surrounding environment (RI) was plotted in Fig. 10. The results obtained in the range of RI = 1.31 to 1.37 indicate an almost linear relationship between these two parameters. The slope of the line fitted to the data was calculated to be 3312.1 nm/RIU, which represents the average spectral sensitivity of the sensor in this range. The coefficient of determination ($R^2$) of 0.9817 also indicates a stable and reliable response of the sensor to the changes in the refractive index. This remarkable linearity in the calibration plot is evidence of the compatibility of the sensor structure design with the principles of the interaction of the optical field and the surface plasmon wave under resonant conditions. Therefore, the proposed sensor shows a desirable performance in applications such as bio-detection, environmental analysis, and precision sensing. To underline the performance of the proposed structure, the results of this research are compared with other related papers. Table 6 shows the sensitivity values for this study and previous research. As shown in Fig. 10, the calibration curve deviates from perfect linearity and has a slope greater than 1 for RI values greater than 1.35. This result is expected due to the nonlinear behavior of the surface plasmon dispersion. This means that at high RI values the coupling efficiency between the surface plasmon mode and the guided mode falls into a saturation region since the effective index of the surface plasmon is similar to that of the guided mode. The β_core and the k_sp phase-matching condition become nonlinear at high analyte indices which results in a somewhat superlinear shift in the resonance wavelength. The previously documented observation of a shift in the resonance wavelength has no effect on the measured sensitivity since the calibration curve is still linear throughout the operating region of the device.

To demonstrate the uniqueness of the development of our sensor, we have compiled where we compare the method of construction, the amount of complexity in producing the sensor, and the methods for detecting wavelength-sensitive changes (in most cases) for a selection of examples of the latest SPR Sensors with our D-shaped fiber sensor. In this Table 5, the route to producing each sensor has been separated into 3 categories, Simple, Moderate and Complex, depending on how many steps were involved to produce each type: (e.g. standard side-polishing and thin-films versus special fiber-drawing, micromachining or nano-patterning). The sensing method

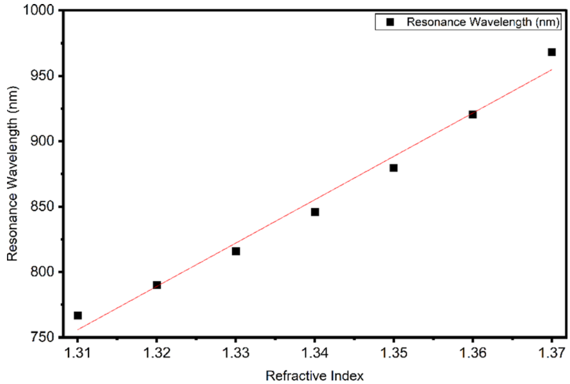


**Fig. 10** Calibration diagram showing the linear relationship between the refractive index of the surrounding medium and the resonant wavelength

**Table 5** Comparison of structure type, fabrication complexity and wavelength sensitivity between the proposed SPR sensor and representative recently reported SPR sensors

| References | Structure type | Fabrication complexity | Sensitivity (nm/RIU) |
|---|---|---|---|
| Your work | D-shaped fiber with Au/$TiO_2$/Ag multilayer and surface nano-grating | Medium – standard side-polishing, thin-film deposition and single-side nano-grating | 5100 |
| [42] | Tapered optical fiber with low-RI liquid-crystal cladding and bimetallic Ag–Au layers (SPR) | High – fiber tapering + bi-metallic coating + LC cell with electrodes | — (RI sensitivity in nm/RIU not explicitly reported) |
| [44] | Dual-channel SPR optical fiber sensor (cladding removed, Ag layer in channel 1, Au layer in channel 2) | Medium – cladding removal + sequential Ag/Au coating | 1200 / 1650 (first / second channel) |
| [45] | Hollow-core graded-index optical fiber SPR sensor with central Ag-coated hole filled by analyte | High – graded-index fiber + central micro-hole + internal Ag coating | 4350 |
| [46] | External-sensing SPR biosensor based on photonic crystal fiber with Au coating | High – micro-structured PCF + selective metal coating | 35,943.22 |
| [47] | Suspended symmetric double-layer gold gratings supporting surface lattice resonances (SLR sensor platform) | Very high – single-step EBL on $Si_3N_4$ membrane + double-side metal gratings | 500.6 |

proposed in this instance presents competitive to superior sensitivity relative to all but one of the above-mentioned sensors; however, it is produced with a much simpler process (side-polishing, coating, light exposure) versus the complex routes to fabrication in the examples evaluated.

Based on the data presented in Table 6, the performance of the proposed sensor is compared to other studies from various aspects. One of the most important performance indicators is the sensitivity, which is reported as 5100 nm/RIU in this study. The half-maximum width in the proposed sensor is reported to be 14.5 nm, which is a suitable value. This value indicates that the surface plasmon resonance in this design has a relatively narrow peak, which helps improve the detection accuracy. Some other studies have reported a FWHM value of 27 nm, which indicates that the spectral resolution in this design is higher than theirs.

**Table 6** Table comparing the performance of the proposed sensor with other works presented in the literature

| Reference | Sensitivity (nm/RIU) | FOM (1/RIU) | FWHM (nm) | RI range |
|---|---|---|---|---|
| [45] | 4350 | 29 | 149 | 1.38–1.49 |
| [52] | 6400 | 37.8 | – | 1.33–139 |
| [53] | 5980 | 173 | 34.5 | 1.33 |
| [54] | 1900 | – | – | 1–1.1.1 |
| [55] | 1770 | 193 | 9.17 | 1.33–1.38 |
| [56] | 2732 | 61 | 45 | 1.33–1.36 |
| [57] | 1587 | 260 | 6.1 | 1.5–1.57 |
| [58] | 500 | 0.1 | 5000 | 1.34–1.341 |
| [59] | 4000 | 80 | 50 | 1.3–1.38 |
| [60] | 5500 | – | – | 1.23–1.29 |
| [61] | 2812 | 78.23 | 35.95 | 1.33–1.34 |
| [25] | 5847 | 111.45 | – | 1.333–1.38 |
| [62] | 7540 | 280 | 27 | 1.33–1.39 |
| This Work | 5100 | 351.7 | 14.5 | 1.31–1.37 |

Another key indicator is the figure of merit, which is reported to be 351.7 $RIU^{-1}$ for the proposed sensor. This value, compared to some studies that reported values of 280 to 500 $RIU^{-1}$, indicates the desirable performance of the sensor in terms of combining high sensitivity and good spectral resolution. The high FoM value means that the proposed sensor is capable of resolving small changes in refractive index and shows optimal performance in biological and chemical applications. The working range also varies in different studies, but the range of 1.31 to 1.41 in the proposed sensor indicates that this design performs well in applications involving biological environments and chemical sensing. Some studies have reported similar working ranges of 1.33 to 1.39, indicating the efficiency of the proposed sensor over a wide range of target analytes.

To assess the stability of the sensor's performance under real construction conditions, a tolerance analysis was performed, in which minor deviations were applied to the thickness of the key layers of the structure. The thickness of the gold, TiO2 and silver layers was changed to ± 5 nm relative to the optimal values (30, 25 and 25 nm respectively) and its effect on the position of the resonant wavelength and the competence number (FOM) was examined. The results showed that the proposed design was relatively resistant to minor construction fluctuations. Especially in the gold layer, deviations beyond ± 4 nm caused significant displacement in the resonance position and a decrease of about 8–12% in the FOM value. In contrast, the TiO2 and silver layers showed more tolerance, and the FOM changes in them remained less than 5%. These results indicate that the optical performance of the proposed structure remains stable even in case of minor errors in the construction process, and common layering techniques with less than 5 nm accuracy are sufficient for its practical implementation.

The reason for the improved performance of this design comes from the combined effects of a multi-layer coating of both Au–$TiO_2$ and Ag as well as utilizing gratings to assist in coupling. The $TiO_2$ layer is of a higher refractive index than other materials; this causes the effective refractive index of the guided mode to be increased. The difference in the effective refractive indices reduces the phase mismatch between the guided modes of Au and $TiO_2$ and the guided modes of SPPs, which allows for better coupling between these two families of MMs. The presence of multiple layers of metal oxide and silver creates a hybrid SPP mode due to the exchange of energy between the long-range SPPs at the Au–$TiO_2$ interface and the highly localized ("confined") short-range SPPs at the $TiO_2$–Ag interface. In addition, this hybrid creation phenomenon produces stronger localization of the electromagnetic fields adjacent to the surface of the sensor element. The presence of the multiple layer grating structure not only provides added surface area, but also provides additional "momentum" to allow for complete matching of the respective phase-matching conditions of the core mode (βcore) to the SPP mode(kSPP). Together, this confinement of fields and the phase-matching condition create deeper resonance dips and higher sensitivity with this configuration than would normally be expected without these structures being present.

The proposed structure of this study has achieved a sensitivity equivalent to 5100 nm/RIU and a significant competence number using the combination of gold–TiO2–silver and surface grating. This increase in performance can be attributed to the synergistic interaction of plasmon modes at several levels, better adaptation of optical impedance and reduction of absorption losses. Also, unlike some complex structures such as optical crystalline fibers or antenna nanostructures, the present structure can be constructed using achievable methods such as layering and lithography, and therefore also has an operational advantage. A tolerance analysis was performed to assess the strength of the proposed design. The tolerance analysis was performed not only on the thicknesses of the $TiO_2$ and metal, but also on various aspects of the grating. The grating period, Λ and the grating depth, h were disrupted by ±5% from their respective optimum values (Λ = 200 nm → 190–210 nm and h = 50 nm → 47.5–52.5 nm); the resonance wavelength, FWHM, sensitivity, and FoM were re-calculated for each perturbed structure. The results indicate that for a ± 5% change in the two grating parameters, the resulting change in sensitivity and FoM will be less than ~5%, with only a small shift in the resonance wavelength. This shows that the multilayer configuration (Au–$TiO_2$–Ag) and associated grating configuration are highly tolerable to manufacturing processes, and are very likely to remain operationally functional under normal manufacturing deviations.

Although the present work is based on numerical simulations, an experimental implementation is planned. The multilayer coating can be deposited using magnetron sputtering, while the 200 nm period grating can be fabricated using nanoimprint lithography or focused-ion-beam milling. The device would then be characterized using a broadband source and an optical spectrum analyzer by monitoring the transmission dip as the analyte RI changes. Practical challenges include maintaining stable fiber alignment, minimizing surface roughness of the metal films, ensuring accurate reproduction of the grating geometry, and achieving uniform thin-film deposition on the D-fiber surface. These factors may introduce wavelength noise or resonance broadening in the fabricated device, but they are well within the capabilities of current fabrication and measurement techniques.

With a peak sensitivity of 5100 nm/RIU and a linewidth of approximately 16 nm, the proposed Au–$TiO_2$–Ag grating-assisted SPR sensor exhibits an estimated refractive-index detection limit on the order of $10^{-6}$ RIU when operated with a standard 0.02 nm-resolution spectrometer. This level of precision enables the detection of trace chemical species, small variations in salinity or contamination in environmental water samples, and low-concentration biomolecular interactions in biosensing scenarios. Therefore, the numerically demonstrated performance is not only of academic interest but also directly relevant to practical chemical and biological sensing applications.

## 6 Conclusion

In this work, a grating-assisted SPR D-shaped fiber sensor employing a multilayer Au–$TiO_2$–Ag stack was numerically designed and optimized to achieve high-performance refractometric sensing. The optimal configuration—30 nm Au, 25 nm $TiO_2$, and 25 nm Ag—was determined by balancing strong plasmonic absorption with minimized resonance linewidth. The final design has a sensitivity of 5100 nm/RIU, a narrow full width at half maximum (FWHM) of 14.5 nm, and a high figure of merit (FOM) of 351.7 within the range of refractive indices of 1.31–1.37, which demonstrates a high degree of accurateness and spectral sharpness of the design. Through parametric analysis and tolerance analysis, it was determined that operation would not vary more than ±5 nm due to fabrication variations. Additionally, through use of the multilayered structure, and the ability to use grating to provide momentum matching, enhanced confinement of the electromagnetic field has been observed when compared to previous broadband SPR fiber sensor designs. The surface of the proposed sensor is amenable to all practical fabrication techniques such as manual polishing, sputtering or physical vapor deposition for surface coating, and nanoimprint or E-beam lithography for grating fabrication. Several environmental perturbations and temperature-induced drifts in RI will be taken into account; these perturbations are predictable and can be compensated for. Experimental building and validation of this model will occur in conjunction with development of biochemical functionalized layers for use in detecting specific biological/environmental agents. Further work may allow for extending the ability of this system to measure multiple parameters at once - therefore allowing simultaneous determination of RI, salinity, temperature, and/or chemical analysis for real-time monitoring applications. With sensitivity reaching 5100 nm/RIU and determining resonance linewidth 14.5 nm, the proposed form represents a projected detection range around $10^{-5}$ RIU. This projected detection range corresponds with typical biological and chemical sensing applications where refractive index change can occur as result of molecular binding or environmental contaminants, such as $10^{-4}$ and $10^{-6}$ RIU; thus, demonstrating that these optimized structures will provide reliable performance within real-world settings (aqueous, biochemical or Environmental monitoring).

**Author Contributions** Design, analysis, and investigation: Pooria Rabiei, writing—original draft preparation: Pooria Rabiei, Writing—review and editing: Mohammad Danaie, Supervision: Kiana Peyvandi, Ali Asghar Ajami, Mohammad Danaie.

**Funding** This article received no funds.

**Data Availability** No datasets were generated or analysed during the current study.

## Declarations

**Conflict of interest** The authors confirm that they have no competing interests nor any conflict of interests. We hereby declare that the work presented in this article is the result of our own research and has not been submitted elsewhere for publication. All the data, simulations, and analyses were carried out independently, and any external sources of information have been duly acknowledged through proper citations. We affirm that the presented findings are original, and any resemblance to existing work is purely coincidental. I further declare that there are no conflicts of interest related to this work.

## References

1. Schasfoort, R. B. (2017). *Handbook of surface plasmon resonance*. Royal Society of Chemistry.
2. Xu, Y., Wu, L., & Ang, L. K. (2018). $\text {MoS} _2 $-based highly sensitive near-infrared surface plasmon resonance refractive index sensor. *IEEE Journal of Selected Topics in Quantum Electronics*, *25*(2), 1–7.
3. Mahmood, A. I. (2018). Design and simulation of surface plasmon resonance sensors for environmental monitoring. *Journal of physics: Conference series.* IOP Publishing.
4. Prinsi, C. B. (2024). Towards a fiber-optic sensor for monitoring bacterial contaminations in water. *Optical fibers and sensors for medical diagnostics, treatment, and environmental applications XXIV.* SPIE.
5. Ibrahim, M. K., Kadhim, S. A., & Fawaz, N. I. (2021). Water pollution fiber sensor based on surface plasmon resonance technique; implementation and characterization. In S. Bala (Ed.), *Journal of physics: Conference series.* IOP Publishing.
6. Daraigan, S. G. (2006). Water pollution monitoring using optical sensor based on transmitted light. *Sensors, and command, control, communications, and intelligence (C3I) technologies for homeland security and homeland defense V.* SPIE.
7. Pesavento, M., et al. (2019). An optical fiber chemical sensor for the detection of copper (II) in drinking water. *Sensors (Basel, Switzerland)*, *19*(23), 5246.
8. Wang, S., Forzani, E. S., & Tao, N. (2007). Detection of heavy metal ions in water by high-resolution surface plasmon resonance spectroscopy combined with anodic stripping voltammetry. *Analytical Chemistry, 79*(12), 4427–4432.
9. Bano, A. (2018). SPR fiber based sensor for long-term monitoring of aqueous media. *IEEE international instrumentation and measurement technology conference (I2MTC).* IEEE.
10. Hlubina, P., Kadulova, M., & Ciprian, D. (2014). Surface plasmon resonance based fiber optic refractive index sensors. *19th Polish-Slovak-Czech optical conference on wave and quantum aspects of contemporary optics.* SPIE.
11. Cunha, N. H., Da, J. P., & Silva (2022). High sensitivity surface plasmon resonance sensor based on a ge-doped defect and d-shaped microstructured optical fiber. *Sensors (Basel, Switzerland)*, *22*(9), 3220.
12. Zhao, C., et al. (2017). Numerical investigation into a surface plasmon resonance sensor based on optical fiber microring. *Photonic Sensors*, *7*(2), 105–112.
13. Dormeny, A. A., Sohi, P. A., & Kahrizi, M. (2019). On the sensitivity of optical fiber surface plasmon resonance based sensor for detection of dielectric analytes using COMSOL multiphysics. *2019 international conference on numerical simulation of optoelectronic devices (NUSOD).* IEEE.
14. Liu, G., et al. (2014). Side-hole plastic optical fiber for testing liquid's refractive index. *IEEE Sensors Journal*, *15*(5), 2902–2905.

15. Gangwar, R. K., Amorim, V. A., & Marques, P. (2019). High performance titanium oxide coated D-shaped optical fiber plasmonic sensor. *IEEE sensors journal*, *19*(20), 9244–9248.
16. Yang, H., et al. (2021). Highly sensitive refractive index sensor based on SPR with silver and titanium dioxide coating. *Optical and quantum electronics*, *53*(6), 341.
17. Mehan, N., et al. (2005). Surface plasmon resonance based refractive index sensor for liquids. *Indian journal of pure & applied physics*, *43*(11), 854–858.
18. Ye, Y., et al. (2022). Portable multihole plastic optical fiber sensor for liquid-level and refractive index monitoring. *IEEE Sensors Journal*, *23*(3), 2161–2168.
19. Wang, S., et al. (2020). Refractive index sensor based on double side-polished U-shaped plastic optical fiber. *Sensors (Basel, Switzerland)*, *20*(18), 5253.
20. Md Yasin, M. Z., et al. (2024). Modelling a D-shaped Sensor for Transformer Oil Refractive Index Detection. *Journal of Advanced Research in Applied Mechanics*, *114*(1), 43–50.
21. Singh, S., & Kaler, R. (2018). Performance analysis of evanescent wave absorption plasmonic optical sensor with COMSOL FEM method simulation. *Procedia Computer Science*, *125*, 376–381.
22. Motogaito, A., et al. (2016). Detecting high-refractive-index media using surface plasmon sensor with one-dimensional metal diffraction grating. *Optics and Photonics Journal*, *6*(7), 164–170.
23. Guzmán-Sepúlveda, J. R., et al. (2013). A highly sensitive fiber optic sensor based on two-core fiber for refractive index measurement. *Sensors (Basel, Switzerland)*, *13*(10), 14200–14213.
24. Ibrahim, M. K., Kadhim, S. A., & Fawaz, N. I. (2020). *Simulation of performance enhancement for water pollution sensor based on fiber optic technique*. in *AIP Conference Proceedings*. AIP Publishing LLC.
25. Dormeny, A. A., Sohi, P. A., & Kahrizi, M. (2020). Design and simulation of a refractive index sensor based on SPR and LSPR using gold nanostructures. *Results in Physics*, *16*, 102869.
26. Kong, L., et al. (2020). Sensitivity-enhanced SPR sensor based on graphene and subwavelength silver gratings. *Nanomaterials*, *10*(11), 2125.
27. Kadhim, R. A. (2020). Optical fiber refractive index sensor based on the SPR using a multiple D-shaped Ag nanowire. *2020 IEEE sensors.* IEEE.
28. Chauhan, M., Das, S., & Singh, V. K. (2022). Design and analysis of Micro-channelled Quasi D-shape optical Fiber plasmonic Sensor. *Journal of Physics: Conference Series*. https://doi.org/10.1088/1742-6596/2357/1/012002
29. Sharma, V., et al. (2023). Graphene/Au/MIP-coated D-shaped optical fiber–based SPR sensor for ethanol detection. *Plasmonics*, *18*(5), 1639–1649.
30. Rahad, R., et al. (2023). Plasmonic refractive index sensing in the early diagnosis of diabetes, anemia, and cancer: An exploration of biological biomarkers. *Results in Physics*, *49*, 106478.
31. Haque, M. A., et al. (2023). Plasmonic sensor for rapid detection of water adulteration in honey and quantitative measurement of lactose concentration in solution. *Results in Physics*, *51*, 106733.
32. Hossea, J. H., & Rugumira, G. (2024). Analytical design of a portable surface plasmon resonance sensor by using a divergence beam for measuring multiple heavy metals and other contamination simultaneously. *International Journal of Multidisciplinary and Current Research, 12*, 200–207.
33. Kadhim, R. A., et al. (2024). D-shaped microfluidic channel bimetallic with a highly sensitive spr ri sensor for a large detection range. *Plasmonics*, *19*(3), 1383–1394.
34. Tuaimah, A. M., et al. (2024). Multi analyte detection based on D-shaped PCF sensor for glucose concentrations sensing. *Optical and Quantum Electronics*, *56*(3), 319.
35. Yan, X., et al. (2024). MnO2-based dual channel surface plasmon resonance fiber sensor for trace glutathione and refractive index detection. *Optics Express*, *32*(5), 8425–8436.
36. Sun, L., et al. (2024). Dual-parameter fiber optic surface plasmon resonance sensor with narrow FWHM based on an incidence angle adjusting method. *Optics Express*, *32*(21), 37480–37491.
37. Rutirawut, T., et al. (2024). Optical fiber-coupled Kretschmann SPR sensor with re-attachable gold nano-thin film sensing chip. *Optics Express*, *32*(22), 39924–39937.
38. Chakraborty, S., et al. (2025). Design analysis and optimization of a twin-core double D-shaped plasmonic sensor for detection of wide-range refractive index. *Journal of Electronic Materials, 54*, 9493–9500.
39. Vayghan, N. S., & Eftekharinia, B. (2022). Refractive index sensor based on surface plasmon resonance excitation in a D-shaped optical fiber coated by tantalum. *Plasmonics*, *17*(6), 2473–2481.
40. Wang, D. (2022). Research on tunable SPR sensors based on WS2 and graphene hybrid nanosheets. *Photonics.* MDPI.
41. Maleki, M., & Soroosh, M. (2023). A low-loss subwavelength plasmonic waveguide for surface plasmon polariton transmission in optical circuits. *Optical and Quantum Electronics*, *55*(14), 1266.

42. Korec, J., Stasiewicz, K., & Jaroszewicz, L. (2022). SPR Sensor Based on Tapered Optical Fiber with a Low Refractive Index Liquid Crystal Cladding. *Engineering Proceedings, 21*(1), 31.
43. Kumar, A., M. V, and, & Gupta, R. (2023). The Effect of Relative In-Plane Twisting in Graphene Bilayer on Sensing Using Surface Plasmon Resonance. *Plasmonics*, *18*(1), 213–224.
44. Nasirifar, R., Danaie, M., & Dideban, A. (2019). Dual channel optical fiber refractive index sensor based on surface plasmon resonance. *Optik*, *186*, 194–204.
45. Nasirifar, R., Danaie, M., & Dideban, A. (2020). Hollow-core graded index optical fiber refractive index sensor based on surface plasmon resonance. *Optical and Quantum Electronics*, *52*(7), 341.
46. Mitu, S. A., et al. (2022). Surface plasmon resonance–based refractive index biosensor: An external sensing approach. *Plasmonics*, *17*(4), 1581–1592.
47. Cen, M. (2022). Plasmonic surface lattice resonances in suspended symmetric double-layer gratings. *Photonics*. https://doi.org/10.3390/photonics9120890
48. Jing, J., et al. (2021). Performance improvement approaches for optical fiber SPR sensors and their sensing applications. *Photonics Research*, *10*(1), 126–147.
49. Lopes, R. N., et al. (2024). Development of an immunocapture-based polymeric optical fiber sensor for bacterial detection in water. *Polymers*, *16*(6), 861.
50. Santos, D., Guerreiro, A., & Baptista, J. M. (2017). SPR optimization using metamaterials in a D-type PCF refractive index sensor. *Optical Fiber Technology*, *33*, 83–88.
51. Sathukarn, A., et al. (2020). The simulation of a surface plasmon resonance metallic grating for maximizing THz sensitivity in refractive index sensor application. *International Journal of Optics*, *2020*(1), 3138725.
52. Kadhim, R. A., et al. (2020). Highly sensitive D-shaped optical fiber surface plasmon resonance refractive index sensor based on Ag-α-Fe 2 O 3 grating. *IEEE Sensors Journal*, *20*(17), 9816–9824.
53. Tabassum, R., & Gupta, B. D. (2016). Influence of oxide overlayer on the performance of a fiber optic SPR sensor with Al/Cu layers. *IEEE Journal of Selected Topics in Quantum Electronics, 23*(2), 81–88.
54. Asgari, S., & Granpayeh, N. (2019). Tunable mid-infrared refractive index sensor composed of asymmetric double graphene layers. *IEEE Sensors Journal, 19*(14), 5686–5691.
55. Su, Y., et al. (2018). Surface-plasmon-resonance-based optical fiber curvature sensor with temperature compensation by means of dual modulation method. *Sensors (Basel, Switzerland)*, *18*(8), 2608.
56. Zakaria, R., et al. (2017). Fabrication and simulation studies on D-shaped optical fiber sensor via surface plasmon resonance. *Journal of Modern optics*, *64*(14), 1443–1449.
57. Rashed, A., et al. (2018). Highly-sensitive refractive index sensing by near-infrared metatronic nanocircuits. *ScieNtific REPORtS*, *8*(1), 11457.
58. Guo, T. (2017). Fiber grating-assisted surface plasmon resonance for biochemical and electrochemical sensing. *Journal of Lightwave Technology*, *35*(16), 3323–3333.
59. Santos, D. F., Guerreiro, A., & Baptista, J. M. (2017). Simultaneous plasmonic measurement of refractive index and temperature based on a D-type fiber sensor with gold wires. *IEEE Sensors Journal*, *17*(8), 2439–2446.
60. Liu, C., et al. (2017). Mid-infrared surface plasmon resonance sensor based on photonic crystal fibers. *Optics express*, *25*(13), 14227–14237.
61. Zakaria, R., et al. (2021). High sensitivity refractive index sensor in long-range surface plasmon resonance based on side polished optical fiber. *Optical Fiber Technology*, *61*, 102449.
62. Gomez-Cardona, N., Reyes-Vera, E., & Torres, P. (2020). High sensitivity refractive index sensor based on the excitation of long-range surface plasmon polaritons in H-shaped optical fiber. *Sensors (Basel, Switzerland)*, *20*(7), 2111.